Commun Nonlinear Sci Numer Simulat 163 (2026) 110535

Contents lists available at ScienceDirect

Communications in Nonlinear Science and Numerical Simulation

journal homepage: www.elsevier.com/locate/cnsns

Research paper

Voltage-induced vortex triplet instability in a liquid crystal cell

R. Gajardo-Pizarro [a,*], M. G. Clerc [b]

[a] Institut de Physique de Nice, Université Côte d'Azur, 17 rue Julien Lauprêtre, Nice, 06200, France
[b] Departamento de Física and Millennium Institute for Research in Optics, Facultad de Ciencias Físicas y Matemáticas, Universidad de Chile, Casilla 487-3, Santiago, Chile

ARTICLE INFO

Keywords:
Nonlinear optics
Nonequilibrium systems
Self-organized structures
Nematic liquid crystal cell

ABSTRACT

We study the stability of a vortex triplet induced by a magnetic ring in a homeotropic nematic liquid crystal cell subjected to an oscillatory electric field. Our main finding is that increasing the electric field amplitude triggers a discontinuous transition in which the central positive vortex annihilates with a neighboring negative vortex, leaving a single positive vortex pinned at the periphery of the magnetic ring. This transition displays hysteresis and bistability, confirming its first-order character. We experimentally quantify the evolution of the vortex separation distance and the associated annihilation dynamics. To understand these observations, we derive an amplitude equation valid near the reorientation instability and obtain a reduced dynamical model for the vortex separation distance. This theoretical framework captures the onset, discontinuity, and hysteresis of the transition, clarifying how magnetic pinning and vortex interactions combine to produce the observed instability and offering insight into the controlled manipulation of topological defects in driven liquid crystal systems.

1. Introduction

Topological defects are localized structures that emerge in a wide variety of non-equilibrium systems, including fluids, magnetic media, optics, and liquid crystals, to mention a few [1–9]. Among this localized structures, vortices constitute a fundamental class of defects characterized by a point-like phase singularity around which such phase rotates. The topological features of vortices govern important phenomena such as defect interaction, annihilation, and self-organization, playing a fundamental role in their stability. Such solutions appear in diverse nonlinear systems, including fluids, semiconductor lasers, chemical oscillators, superconductors, predator-prey systems, among others [9–13].

Nematic liquid crystals offer an exceptionally versatile platform for investigating vortex dynamics under external forcing [13,14]. Their continuum elasticity, well-defined topological defect structure, and strong, tunable response to electric, magnetic, and optical fields make them uniquely suited for controlled studies of driven vortex interactions and instabilities. In homeotropic nematic liquid crystal cells with negative dielectric anisotropy, the application of a vertical electric field above the Fréedericksz threshold induces molecular reorientation and the formation of vortex pairs with opposite topological charge [13–15]. These vortices interact and may annihilate in order to minimize the free energy of the system. When an additional magnetic field with a non-uniform spatial distribution is applied, the defect dynamics can be strongly modified through pinning effects and boundary-induced topological constraints.

A relevant reported example is obtained by placing a magnetic ring on top of a nematic liquid crystal cell [16]. The magnetic field generated induces boundary constraints that generates and stabilizes a vortex triplet composed of a central positive vortex and

* Corresponding author.
E-mail address: roberto.gajardo.p@ug.uchile.cl (R. Gajardo-Pizarro).

https://doi.org/10.1016/j.cnsns.2026.110535

Available online 8 July 2026

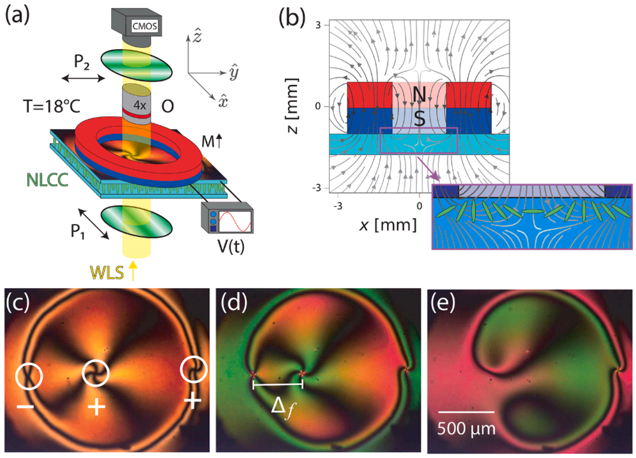

Fig. 1. Voltage-induced vortex triplet instability. (a) Schematic representation of the experimental setup. A nematic liquid crystal cell (NLCC) is subjected to the influence of a magnetic ring (M) and an oscillatory electric field generated by a sinusoidal voltage $V(t) = V_0 \sin(\omega t + \varphi_0)$, where V_0 and ω denote the amplitude and frequency of the applied voltage, and φ_0 is an arbitrary phase. P_1 and P_2 are linear crossed polarizers. The sample is illuminated by a white light source (WLS). A CMOS camera is used to monitor the liquid crystal cell through a microscope objective (O). The green rods schematically represent the average molecular orientation. All experiments were conducted at room temperature $T = 18 \circ C$. (b) Schematic representation of the magnetic field lines near the magnetic ring and their effect on the NLC molecules. The molecular reorientation provides the boundary conditions necessary for the formation of a vortex triplet. (c)-(e) Snapshots of the NLC corresponding to different equilibrium states for different values of V_0 (3.25 V, 3.95 V, and 4.95 V, respectively). Panels (c) and (d) display a vortex triplet, while panel (e) illustrates a single vortex. The white circles mark the vortices and their respective topological charges. Δ denotes the distance between the nearest vortices.

two peripheral vortices of opposite charge (see Fig. 1). Previous studies showed that the vortex triplet remains as the stationary equilibrium state of the system for low intensity of the electric field applied [17], and this structure may destabilize into a vortex lattice under low-frequency forcing [18].

In this work, we demonstrate that the vortex triplet induced by a magnetic ring undergoes a discontinuous transition to a single positive vortex as the amplitude of the applied electric field is varied (cf. Fig. 1). Through combined experimental and theoretical analysis, we show that increasing the driving voltage progressively reduces the separation between the central positive vortex and the adjacent negative vortex. At a critical threshold, these two vortices annihilate, leaving a solitary positive vortex pinned near the inner edge of the magnetic ring. The transition exhibits hysteresis and bistability, consistent with a first-order instability. To grasp these observations, we derive an amplitude equation valid near the reorientation instability and obtain a reduced dynamical model for the vortex separation distance. This theoretical framework captures the onset, discontinuity, and hysteresis of the transition, and the resulting predictions and numerical simulations show both qualitative and quantitative agreement with the experimental measurements.

2. Experimental setup

To generate a vortex triplet, we employ a nematic liquid crystal cell (NLCC) subjected to an oscillatory electric field and a magnetic ring [16]. Fig. 1a shows a schematic representation of the experimental setup. An empty cell, manufactured by Instec, consist of two thin glass plates with transparent indium tin oxide (ITO) electrodes of thickness 0.08 μm, separated by a gap of d = 75 μm. The inner surfaces of the glass plates are treated to ensure homogeneous homeotropic anchoring of the liquid crystal. By capillarity, the cell is filled with the nematic liquid crystal LC-BYVA-01 (Instec), characterized by a negative dielectric anisotropy $\epsilon_a = -4.89$ Fm^{-1}, birefringence $\Delta n = n_e - n_0 = 0.1$, rotational viscosity $\gamma = 204$ mPa·s, and elastic constants $K_1 = 17.65$ pN (splay) and $K_3 = 21.39$ pN (bend). The magnetic anisotropy χ_a has not yet been measured. A neodymium magnetic ring producing a surface field of 3200 G, with rectangular cross-section, outer radius $R_{\text{out}} = 7$ mm, inner radius $R_{\text{out}} = 2$ mm, and thickness $h = 7$ mm, is placed on top of the NLCC. The sample is mounted in an Olympus BX51 microscope, sandwiched between two crossed linear polarizers and illuminated with white light from a halogen lamp, allowing observation via polarized optical microscopy (POM). A sinusoidal voltage $V(t)$ of frequency ω and amplitude V_0 is applied to the NLCC, with V_0 above the critical reorientation threshold, the *Fréedericksz voltage* [15], ranging between 3.05 and 4.25 V. The temporal evolution of the liquid crystal cell is monitored with a complementary metal-oxide-semiconductor (CMOS) camera (Thorlabs DCC1645C), focusing on the central region of the magnetic ring. all experiments were conducted at room temperature $T = 18 \circ C$.

3. Experimental observations

When the magnetic ring is mounted on the homeotropic NLCC, the magnetic field exerts a torque on the molecules inside. This torque alone is insufficient to overcome the elastic resistance and induce molecular reorientation. However, when an oscillatory volt-

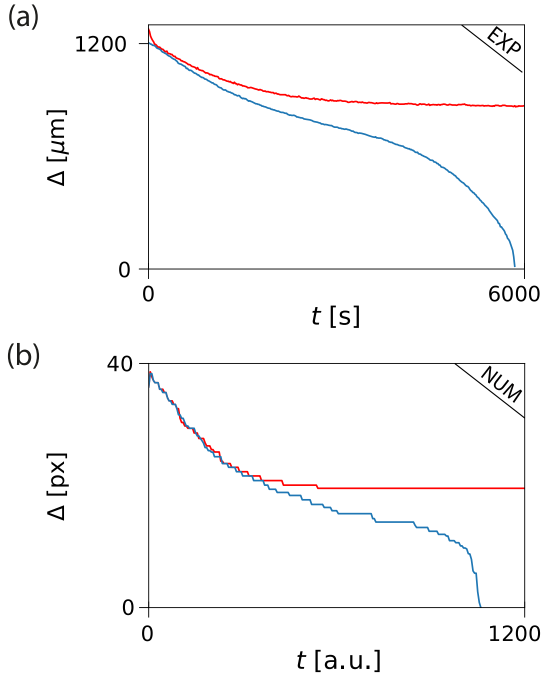

Fig. 2. Evolution of the vortex separation distance Δ over time in (a) experiments and (b) numerical simulations of Eq. (7) with parameters $a = 1$, $\gamma = 1$, $\delta = 0$, $m_0 = 200$, $z = 28$, $\sigma = 28$, and $\ell_0 = 1$. The red curves correspond to cases below the critical transition value ($V_0 < V_c$ and $\mu_0 < \mu_c$), where the separation distance asymptotically converges to a nonzero equilibrium value $\Delta_f \neq 0$ within a relaxation time τ. The cyan curves correspond to cases above the critical value ($V_0 > V_c$ and $\mu_0 > \mu_c$), where the equilibrium separation distance Δ_f decays to zero following vortex annihilation after a characteristic time t_f. In experiments, the relaxation time is measured as $\tau \approx 2 \times 10^3$ s, while the annihilation time is $t_f \approx 6 \times 10^3$ s.

age $V(t) = V_0 \sin(\omega t + \varphi_0)$ is simultaneously applied, the magnetic ring produces an effect that lowers the threshold for reorientational instability, allowing it to occur at voltages V_0 below the Fréedericksz voltage. Due to the non-uniformity of the magnetic field, the emergent structure observed after molecular reorientation is a *vortex triplet* [16], characterized by a positively charged vortex located near the center of the ring, and two flanking vortices of opposite topological charges (see Fig. 1c).

Starting from sufficiently low values of the applied voltage amplitude V_0, the vortex triplet constitutes the equilibrium state of the system. To characterize the evolution of this structure, we define $\Delta(t)$ as the instantaneous separation between the central positive vortex and the adjacent negative vortex (cf. Fig. 1). For fixed values of V_0, the system relaxes toward a stationary configuration characterized by an equilibrium distance Δ_f. As the voltage amplitude increases, the equilibrium distance Δ_f decreases progressively, indicating that the central positive vortex moves closer to the neighboring negative vortex (see Fig. 1c,d). Above a critical voltage V_c, the separation distance vanishes and the two vortices annihilate, leaving a single positive vortex located near the inner edge of the magnetic ring (Fig. 1e). Fig. 2 shows the temporal evolution of the separation distance $\Delta(t)$ for values of V_0 below and above the critical voltage V_c. For $V_0 < V_c$, the system relaxes toward a finite equilibrium separation $\Delta_f \neq 0$, whereas for $V_0 > V_c$, the separation distance decays to zero following vortex annihilation. Conversely, when starting from the single-vortex configuration and decreasing the voltage amplitude V_0, the vortex-triplet structure reappears at a lower critical voltage $V_s < V_c$. The resulting hysteresis cycle, shown in Fig. 3a, reveals the coexistence of two stable states over a finite voltage interval and constitutes the experimental signature of a first-order transition [19].

The dynamics of the vortex separation can be phenomenologically described by

$$\dot{\Delta} = -a_1 \Delta + a_2 \Delta^2 - a_3 \Delta^3, \tag{1}$$

where $\{a_1, a_2, a_3\}$ are phenomenological coefficients, with a_1 acting as the bifurcation parameter. The equilibrium states of this model are $\Delta_f^0 = 0$ and

$$\Delta_f^{\pm} = \frac{a_2 \pm \sqrt{a_2^2 - 4a_1 a_3}}{2a_3}. \tag{2}$$

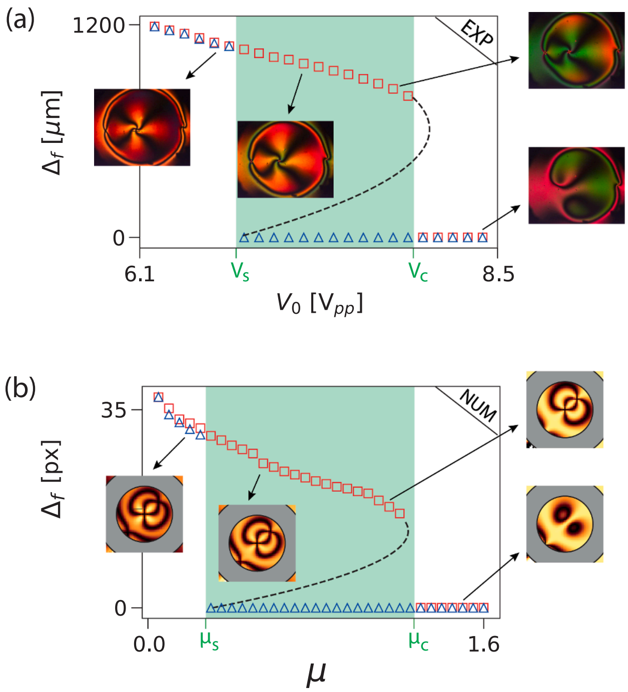

Fig. 3. Transition from a vortex triplet to a single vortex. (a) Experimental and (b) numerical bifurcation diagrams of the transition between a vortex triplet and a single vortex. In both plots, the equilibrium distance Δ_f between vortices is shown on the ordinate as a function of the bifurcation parameter on the abscissa. The shaded region indicates the bistability domain. The numerical bifurcation diagram is obtained by simulating the amplitude equation [Eq. (7)] with parameters $a = 1$, $\gamma = 1$, $\delta = 0$, $m_0 = 200$, $z = 28$, $\sigma = 28$, and $\ell_0 = 1$. Red and blue markers correspond to increasing and decreasing applied voltage V_0 in experiments, or equivalently the bifurcation parameter μ in simulations. Insets display representative snapshots or colormaps for the respective parameter values. Dashed curves denote unstable solutions, obtained from the equilibrium condition in Eq. (1).

Here, Δ_f^0 corresponds to the single-vortex state, while Δ_f^+ represents the triplet configuration. For $a_1 > 0$, the solution Δ_f^0 is stable. By fitting the experimental data for Δ_f to the expression above, the coefficients $\{a_1, a_2, a_3\}$ can be determined. The dashed curve in Fig. 3a is obtained from these fitted parameters.

In brief, the system exhibits either a vortex triplet or a single vortex depending on the applied voltage amplitude V_0. The transition between these two states is discontinuous and of first-order type. In the following section, we provide a theoretical framework to explain the origin of this transition.

4. Theoretical description

To describe the vortex triplet dynamics, we derive an amplitude equation valid in the vicinity of reorientational transition, Fréedericksz transition [15]. Specifically, the liquid crystal molecules, which remains in the nematic phase and preserves a well-defined local orientational order, transition from the homeotropic state where they are oriented parallel to the axis orthogonal to the cell walls, to a configuration where they are tilted away from this axis. In this framework, the local state of the liquid crystal is described by the director vector $\vec{n}(\vec{r}, t)$, an unit vector field representing the average molecular orientation at position $\vec{r}$ and time t. Since nematic liquid crystal molecules are only weakly tilted from the $\hat{z}$ axis after reorientational transition (Fig 1a), backflow effects can be neglected [13].

The orientational dynamics of the nematic liquid crystal result from the competition between elastic distortions and the tendency of the molecules to align with externally applied electric and magnetic fields. Spatial deformations of the director field generate restoring forces that increase the elastic free energy, whereas the coupling to the external fields favors orientations parallel to the directions selected by the dielectric and magnetic anisotropies of the material. The dynamical evolution and equilibrium configurations of the system therefore follow from the minimization of the total free energy, described within the continuum theory of nematics by the Frank–Oseen elastic energy together with the electromagnetic contribution to the free energy [13,14].

$$\mathcal{F}[\vec{n}] = \frac{1}{2}\int \Big\{ K_1(\nabla\cdot\vec{n})^2 + K_2(\vec{n}\cdot(\nabla\times\vec{n}))^2$$

$$+K_3(\vec{n}\times(\nabla\times\vec{n}))^2 - \epsilon_a(\vec{n}\cdot\vec{E})^2 - \chi_a(\vec{n}\cdot\vec{B})^2 \Big\} dV, \tag{3}$$

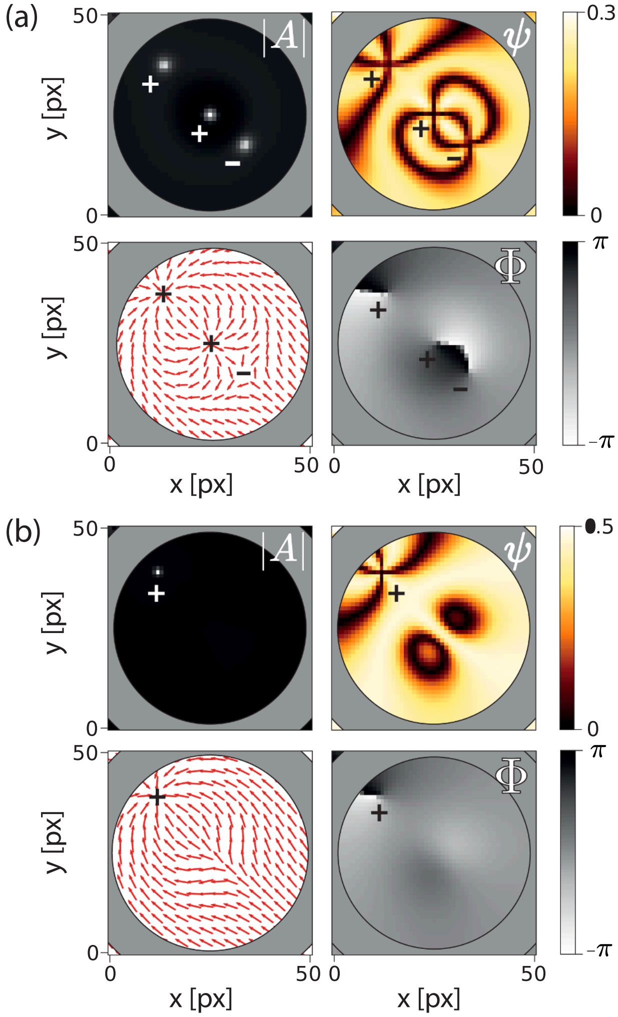

Fig. 4. Numerical simulations of the topologically driven Ginzburg-Landau Eq. () were performed with parameters $\gamma = 1$, $\delta = 0$, $m_0 = 200$, $z = 28$, $\sigma = 28$, and $\ell_0 = 1$. The fields displayed are defined as follows: the amplitude field $|A| = \sqrt{(\mathrm{Re}(A))^2 + (\mathrm{Im}(A))^2}$, the polarization field $\psi = \mathrm{Re}(A)\mathrm{Im}(A)$, arrows representing the orientation of the projection of $\vec{n}$ onto the observation plane, and the phase field $\Phi = \mathrm{arctan2}(\mathrm{Im}(A), \mathrm{Re}(A))$. The bifurcation parameter values used are (a) $\mu_0 = 0.5$ ($\mu_0 < \mu_c$) and (b) $\mu_0 = 1.5$ ($\mu_0 > \mu_c$).

where K_1, K_2, and K_3 are the elastic constants associated with splay, twist, and bend distortions, respectively, ϵ_a and χ_a are the dielectric and magnetic anisotropy of the liquid crystal, $\vec{E} = E_z(t)\hat{z} \approx -(V(t)/d)\hat{z}$ is the vertical oscillatory electric field generated by the applied voltage $V(t)$, and $\vec{B}(r, z) = B_r\hat{r} + B_z\hat{z}$ is the magnetic field produced by the ring, axially symmetric with respect to $\hat{z}$. Here, $\{r, \phi, z\}$ denote cylindrical coordinates with origin at the center of the magnetic ring, with z along the vertical axis. Fig. 1b shows a schematic representation of the magnetic field structure.

The magnetic field generated by the ring has the explicit form [16]

$$\vec{B}(r, z) = m_0 \left[\frac{3zr\hat{r} + (3z^2 + \sigma)\hat{z}}{(r^2 + z^2)^{5/2}} - \frac{\ell_0 \hat{z}}{(r^2 + z^2)^{3/2}} \right] + b_0 \hat{z} \tag{4}$$

where σ, b_0 and ℓ_0 are phenomenological parameters (with dimensions m^2, T, and dimensionless, respectively) that account for geometric features of the magnetic ring, and m_0 is a constant with dimensions of permeability per magnetic moment. Due to the azimuthal symmetry of the ring, the magnetic field is independent of the azimuthal coordinate ϕ.

The dynamics of the director is governed by the minimization of the free energy $\mathcal{F}$ under the constraint $|\vec{n}| = 1$. Accordingly, the evolution of the director satisfies [13]

$$\gamma \frac{d\vec{n}}{dt} = -\frac{\delta \mathcal{F}}{\delta \vec{n}} + \vec{n}\left(\vec{n} \cdot \frac{\delta \mathcal{F}}{\delta \vec{n}} \right), \tag{5}$$

where γ denotes the rotational viscosity of the material [20]. Near the reorientational instability, the director dynamics can be approximated using the ansatz

$$\vec{n}(r,\phi,z;t) \approx \begin{pmatrix} \mathrm{Re}[A(r,\phi,t)]\sin(\frac{\pi z}{d}) \\ \mathrm{Im}[A(r,\phi,t)]\sin(\frac{\pi z}{d}) \\ 1-\frac{|A|^2}{2}\sin^2(\frac{\pi z}{d}) \end{pmatrix} + \text{H.O.T.}, \tag{6}$$

where $A(r,\phi;t)$ is the complex amplitude of the critical mode describing the projection of $\vec{n}$ onto the xy−plane, d is the cell thickness, and H.O.T. denotes higher-order terms in the critical amplitude.

Substituting the ansatz (6) into Eq. (5) and performing straightforward calculations yields to the amplitude equation for A

$$\gamma\partial_t A = (\mu_0+\mu_1)A - aA|A|^2 + \nabla_\perp^2 A + \delta\partial_{\eta\eta}\bar{A} + f e^{i\phi} \tag{7}$$

where $\mu_0 = -K_3(\pi/d)^2 - \epsilon_a(V_0/d)^2$ is the bifurcation parameter associated with the electrical Fréedericksz transition, $\mu_1(r) = -\chi_a B_z^2(r,z_0)$ represents an inhomogeneous correction due to the magnetic field, $a(r) = [(4K_1-6K_3)(\pi/d)^2 - 3\epsilon_a(V_0/d)^2 - 3\chi_a B_z^2(r,z_0)]/4$ accounts for nonlinear inhomogeneities, z_0 is the height of the NLCC, $\delta = (K_1-K_2)/(K_1+K_2)$ quantifies elastic anisotropy, $\partial_\eta = \partial_x + i\partial_y$ is the Wirtinger derivative, and $f(r) = 4\chi_a B_r(r,z_0)B_z(r,z_0)/\pi$ measures the strength of the topological forcing. Spatial coordinates are rescaled as $\vec{r} \to \vec{r}\sqrt{2/(K_1+K_2)}$. Eq. (7), known as the topologically driven Ginzburg-Landau Equation [21], is valid in the asymptotic regime $\mu_0 \ll 1$ with scaling $\mu_0 \sim \mu_1$, $A \sim \mu_0^{1/2}$, $\partial_\eta \sim \mu_0^{1/2}$, $\partial_t \sim \mu_0/\gamma$, and $f \sim \mu_0^{3/2}$, while a and δ remain of order unity. A detailed derivation of the Eq. (7) and parameter mapping to physical quantities is provided in Ref. [22] for the case of having a photosensitive wall or having a magnetic ring in the overdamped limit [18].

The amplitude Eq. (7) has been successfully applied to explain diverse phenomena in liquid crystal systems under high-frequency electric fields, including vortex induction via anisotropy-stabilized light-matter interaction [22,23], symmetry breaking of nematic umbilical defects [24], transitions between standard and shadow vortices [21,25,26], and the emergence of optical vortex lattices [27]. In particular, this amplitude equation provides a framework to study the dynamics and self-organization of magnetic-field-induced vortex triplets in nematic liquid crystal cells [16].

4.1. Vortex triplet instability

Numerical simulations of the amplitude Eq. (7) were carried out using a finite-element solver written with the commercial FlexPDE software. The simulations employed an unstructured triangular mesh with adaptive refinement in both space and time. To ensure sufficient resolution of the vortex structures, the computations were performed in a circular domain of radius 50, subject to Neumann boundary conditions. The adaptive refinement strategy concentrated mesh elements in regions with large field gradients, thereby improving accuracy while maintaining computational efficiency. The corresponding FlexPDE input files are available from the authors upon reasonable request.

Fig. 4a shows a typical vortex triplet obtained from these simulations. The chart displays the amplitude field $|A|$, the polarization field $\psi = \mathrm{Re}(A)\mathrm{Im}(A)$, the unit-vector representation of the complex field (with horizontal and vertical components proportional to $\mathrm{Re}(A)$ and $\mathrm{Im}(A)$, respectively), and the phase field $\Phi = \mathrm{arctan2}(\mathrm{Im}(A), \mathrm{Re}(A))$. The polarization field ψ qualitatively reproduces the intensity patterns observed experimentally under crossed linear polarizers, since the transmitted optical intensity I depends on the local molecular orientation within the liquid-crystal director plane [28]. In particular, the intensity follows $I = I_0\sin^2(\Phi)$, where I_0 is the incident beam intensity and Φ denotes the local director rotation. Then, the intensity can be expressed as $I = I_0\sin^2(\Phi) = 2I_0 Im(A)Re(A)/|A|^2 = 2I_0\psi/|A|^2$. Therefore, the transmitted intensity is proportional to the polarization field. From the simulations, one observes that the central vortex remains dynamically linked to one of the peripheral vortices, a connection clearly manifested in both the polarization and phase fields. These vortices are connected by a phase-discontinuity line that is difficult to visualize directly in experiments, although its presence can be inferred through spatially resolved polarimetry [29] or interferometry [30]. The remaining vortex is connected to the system boundary, a behavior also observed experimentally (see insets in Fig. 3a). By increasing the bifurcation parameter μ_0, the central vortex and its connected peripheral counterpart approach each other. The equilibrium separation distance between the nearest connected vortices is denoted Δ_f. Fig. 3b shows how Δ_f varies with μ_0. At a critical value μ_c, the vortices collide and annihilate, leaving a single vortex near the boundary of the system. This solitary vortex persists as μ_0 increases further, as illustrated in Fig 4b. Conversely, when μ_0 is decreased from the single-vortex state, the solitary vortex remains stable until $\mu_0 = \mu_s$. At this point, a pair of vortices re-emerges, reconstructing the triplet, while further decreasing μ_0 preserves the triplet configuration. Thus, the simulations reveal a hysteresis loop, consistent with experimental observations (cf. Fig. 3).

4.2. Vortex interaction and bifurcation diagram

To shed light on the bifurcation diagram of the different vortex configurations, we characterize the interaction between vortices. For the analytical calculations, we use the magnetic field expression (4) to obtain the components B_r and B_z in the nematic liquid crystal plane at height z_*. For simplicity, we set $b_0 = 0$ in the magnetic field and $\delta = 0$ in the amplitude Eq. (7). To describe vortex interactions, we assume that vortices are sufficiently separated compared to the core length, where the amplitude tends to zero. We consider the following ansatz for the amplitude $|A|$ of the order parameter

$$|A|(\vec{r},t) = R_v(|\vec{r}-\epsilon\vec{r}_0|) + R_p(|\vec{r}-\vec{r}_p|) + R_m(|\vec{r}-\vec{r}_m|), \tag{8}$$

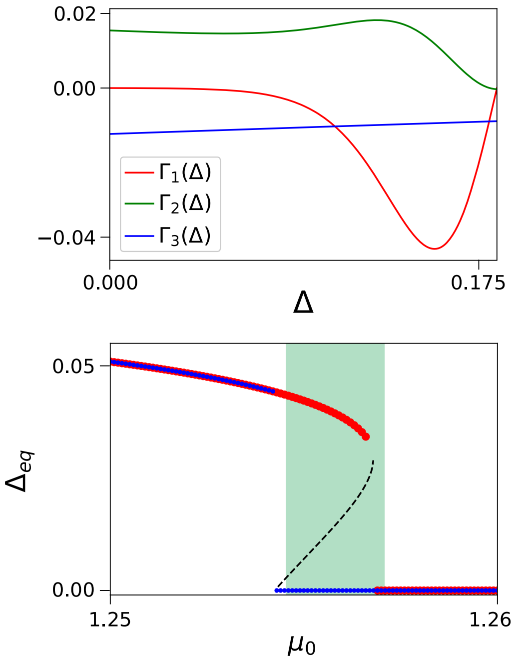

Fig. 5. Characterization of interaction coefficients and bifurcation diagram. (a) Functions Γ_1, Γ_2 and Γ_3 plotted as a function of the separation distance Δ. The red, green and blue curves correspond to Γ_1, Γ_2 and Γ_3, respectively. (b) Bifurcation diagram obtained from Eq. (11), showing a first-order transition between a vortex triplet and a single vortex. The red and blue markers represent the equilibrium separation distance as a function of the bifurcation parameter μ_0, for increasing and decreasing values, respectively. The shaded region indicates the bistability domain.

where $R_v(\vec{r})e^{i\theta(\vec{r})}$ is the vortex solution of Eq. (7), $\vec{r}_0$ is the position of the central positive vortex, separated by $\Delta(t) = |\vec{r}_0 - \vec{r}_m|$ from the peripheral vortex with which it collides. Indices p and m denote the peripheral positive and negative vortex, located at $\vec{r}_p(t)$ and $\vec{r}_m(t)$, respectively. As shown in Fig. 1, the local amplitude and phase of the central vortex are only weakly affected by the others, so the peripheral vortices can be treated as small perturbations decaying exponentially with distance

$$R_p(|\vec{r}-\vec{r}_p|) \approx -\sqrt{\mu_0} + \alpha_p e^{-\lambda|\vec{r}-\vec{r}_p|},$$

$$R_m(|\vec{r}-\vec{r}_m|) \approx \sqrt{\mu_0} + \alpha_m e^{-\lambda|\vec{r}-\vec{r}_m|}, \tag{9}$$

where α_p, α_m and λ characterize the asymptotic behavior of the peripheral vortices. Thus, the ansatz for the order parameter becomes

$$A(\vec{r},t) = [R_v(|\vec{r}-\epsilon\vec{r}_0|) + \tilde{\alpha}(\vec{r}) + \epsilon W]e^{i\theta(\vec{r})}, \tag{10}$$

with $\tilde{\alpha}(\vec{r}) = \alpha_m e^{-\lambda|\vec{r}-\vec{r}_m|} - \alpha_p e^{-\lambda|\vec{r}-\vec{r}_p|}$, and W denoting higher-order corrections.

Substituting the ansatz (10) into Eq. (7), using the magnetic field approximation (4), linearizing in W, and imposing a solvability condition, we obtain the dynamic equation for the separation distance Δ

$$\dot{\Delta} = \Gamma_1(\Delta) + \mu_0^{-1/2}\Gamma_2(\Delta) + \mu_0^{1/2}\Gamma_3(\Delta), \tag{11}$$

where Γ_1 and Γ_2 represent magnetic field effects, while Γ_3 accounts for peripheral vortex interactions. Explicit expressions for these functions are provided in Appendix A, and their behavior is illustrated in Fig. 5a.

From Eq. (11) and Fig. 5a, one can identify the roles of the different contributions in the vortex triplet instability as μ_0 increases. Magnetic field effects (Γ_1 and Γ_2) dominate at low μ_0, allowing vortices to remain separated due to pinning [9]. At larger μ_0, peripheral vortex interactions (Γ_3) become dominant, driving vortex pair annihilation under strong electric fields. Importantly, Eq. (11) predicts a first-order transition as μ_0 varies, consistent with the bifurcation diagram shown in Fig. 5b.

5. Conclusions

We experimentally and theoretically investigated the stability of a vortex triplet induced by a magnetic ring in a homeotropic nematic liquid crystal cell subjected to an oscillatory electric field. By increasing the applied voltage amplitude, equivalently the electric-field amplitude across the cell, the system undergoes a transition from a vortex triplet to a single-vortex state through the annihilation of two vortices with opposite topological charge. The transition exhibits hysteresis and bistability, revealing its first-order character.

The transition occurs at different critical voltages depending on whether the voltage is increased or decreased, giving rise to a hysteresis cycle between the triplet and single-vortex configurations. To account for these observations, we employed an amplitude equation derived near the Fréedericksz instability that incorporates both the electric forcing and the spatial inhomogeneity induced by the magnetic field. Numerical simulations reproduce the existence of the vortex triplet, the annihilation process, and the associated hysteresis loop observed experimentally. Within this framework, we further derived a reduced dynamical equation for the vortex separation distance, which identifies the competition between magnetic pinning and vortex interactions as the mechanism driving the instability.

Previous studies have established and confirmed experimentally interaction laws for vortex pairs at small separations [9,31]. At larger separations, however, vortex interactions are strongly modified by system inhomogeneities induced by external electric or magnetic fields. Our observations provide new insight into how each external field contributes to vortex interactions, highlighting the interplay between pinning effects at low voltages and pairwise annihilation at higher voltages. This work thus advances the understanding of topological defect dynamics in nematic liquid crystals and their control via external fields.

CRediT authorship contribution statement

R. Gajardo-Pizarro: Writing – review & editing, Writing – original draft, Investigation, Funding acquisition, Data curation; **M. G. Clerc:** Writing – review & editing, Writing – original draft, Supervision, Resources, Investigation.

Declaration of competing interest

The authors declare that they have no known competing financial interests or personal relationships that could have appeared to influence the work reported in this paper.

Acknowledgements

Authors are thankful for the financial support of ANID-Millennium Science Initiative Program-ICN 17_012, Chile (MIRO) and FONDECYT, Chile Project No. 1260307. R. G-P. thanks the financial support of ANID by Beca Doctorado Nacional 2022–21221819.

Data availability

Data will be made available on request.

Supplementary material

Supplementary material associated with this article can be found in the online version at 10.1016/j.cnsns.2026.110535.

Appendix A. Derivation of vortex interaction equation

Let us consider the limiting case of a liquid crystal cell without the magnetic ring and neglecting anisotropy, the nematic liquid crystal cell under the effect of a driving voltage is modeled by using the Ginzburg-Landau equation (GLE)

$$\partial_t A = \mu A - A|A|^2 + \nabla^2 A. \tag{A.1}$$

In this equation, $\mu = -K_3(\pi/d)^2 - \varepsilon_a E^2$ is the bifurcation parameter for the Fréedericksz reorientation transition. If we consider a magnetic ring over the NLCC with magnetization perpendicular to the cell and using the center of the ring as coodinate origin, the system will be under the influence of a magnetic field of the form

$$\vec{B}(r,z) = B_r(r,z)\hat{r} + B_z(r,z)\hat{z}, \tag{A.2}$$

with

$$B_r(r,z) = \frac{3M_0 rz}{4\pi(r^2+z^2)^{\frac{5}{2}}}, \tag{A.3}$$

$$B_z(r,z) = \frac{M_0}{4\pi}\left(\frac{3z^2+\sigma}{(r^2+z^2)^{\frac{5}{2}}} - \frac{\ell_0}{(r^2+z^2)^{\frac{3}{2}}}\right). \tag{A.4}$$

The magnetic field exerts a torque on the molecules, producing a small spatially dependent perturbation $g(\vec{r}) = -\chi_a B_z^2(r,z_*)$ of the bifurcation parameter μ, as well as a correction $f(\vec{r})e^{i\theta} = -4\chi_a B_r(r,z_*)B_z(r,z_*)e^{i\theta}/\pi$ to the GLE. Here, z_* denotes the height of the

NLCC relative to the central plane of the magnetic ring (which will be omitted from now on for brevity). Because the magnetic field is non-uniform, the resulting torque, and therefore the perturbations, varies in magnitude across the cell. Using $\delta_0 \ll 1$ as an expansion parameter, the topologically driven GLE takes the form

$$\partial_t A = \left[\mu + \delta_0 g(\vec{r})\right] A - A|A|^2 + \nabla^2 A + \delta_0 f(\vec{r}) e^{i\theta}. \tag{A.5}$$

The complete configuration consists of a central positive vortex connected to two vortices of opposite topological charge, arranged such that the three defects lie approximately along a straight line. We further assume that the terms of order δ_0 act as perturbations of comparable magnitude. Under these assumptions, the ansatz for the vortex dynamics takes the form

$$A(\vec{r},t) = R_v(\vec{r} - \delta_0 \vec{r}_0) e^{i\theta(\vec{r})} + R_+(\vec{r} - \vec{r}_p) e^{i\theta_+(\vec{r})}$$

$$+ R_-(\vec{r} - \vec{r}_m) e^{i\theta_-(\vec{r})} + \delta_0 W. \tag{A.6}$$

where $R_v(\vec{r})$, R_+, and R_- denote the amplitudes of the vortex solutions of Eq. (A.1) at the central position and at the two antipodal locations, respectively. The set $\{\vec{r}_0, \vec{r}_p, \vec{r}_m\}$ represents the positions of the central vortex, the peripheral positive vortex, and the negative vortex. We assume that the influence of the peripheral vortices decays exponentially with their separation from the central positive vortex. In addition, we take the phase field to be $\theta(\vec{r}) = \mathrm{atan}(\vec{r} - \delta_0 \vec{r}_0)$. Under these assumptions, the vortex amplitudes become

$$R_+(\vec{r} - \vec{r}_p) e^{i\theta_+(\vec{r})} \approx \left(\sqrt{\mu} + a_+ e^{-\lambda|\vec{r} - \vec{r}_p|}\right) e^{i0}, \tag{A.7}$$

$$R_-(\vec{r} - \vec{r}_m) e^{i\theta_-(\vec{r})} \approx \left(\sqrt{\mu} + a_- e^{-\lambda|\vec{r} - \vec{r}_m|}\right) e^{i\pi}. \tag{A.8}$$

Using the above approximations, the ansatz (A.6) can be rewritten as

$$A(\vec{r},t) \approx \left(R_* + \delta_0 W\right) e^{i\theta},$$

with

$$R_* = R_v(\vec{r} - \delta_0 \vec{r}_0) + a_+ e^{-\lambda|\vec{r} - \vec{r}_p|} - a_- e^{-\lambda|\vec{r} - \vec{r}_m|}. \tag{A.9}$$

The different terms of Eq. (A.1) are represented as follows

$$\partial_t A = -\delta_0\, \dot{\vec{r}}_0 \cdot (\nabla R_v)\, e^{i\theta}, \tag{A.10}$$

$$\begin{aligned} A|A|^2 \approx \Big[& R_v^3 + 3R_v^2\Big(a_+ e^{-\lambda|\vec{r} - \vec{r}_p|} - a_- e^{-\lambda|\vec{r} - \vec{r}_m|}\Big) \\ & + \delta_0 R_v^2 (2W + \overline{W})\Big] e^{i\theta}, \end{aligned} \tag{A.11}$$

$$\begin{aligned} \nabla^2 A = \Big[& \nabla^2 R_v + \lambda^2\Big(a_+ e^{-\lambda|\vec{r} - \vec{r}_p|} - a_- e^{-\lambda|\vec{r} - \vec{r}_m|}\Big) \\ & + \delta_0\, \nabla^2 W\Big] e^{i\theta}. \end{aligned} \tag{A.12}$$

When all the preceding calculations are taken into account, the 0th-order equation becomes

$$\mu R_v - R_v^3 + \nabla^2 R_v = 0. \tag{A.13}$$

The δ-order equation takes the form

$$\begin{aligned} -\dot{\vec{r}}_0 \cdot (\nabla R_v) = {} & \mu\Big(a_+ e^{-\lambda|\vec{r} - \vec{r}_p|} - a_- e^{-\lambda|\vec{r} - \vec{r}_m|}\Big) + R_v g(\vec{r}) \\ & - 3R_v^2\Big(a_+ e^{-\lambda|\vec{r} - \vec{r}_p|} - a_- e^{-\lambda|\vec{r} - \vec{r}_m|}\Big) \\ & - 2R_v^2 W - R_v^2 \overline{W} \\ & + \lambda^2\Big(a_+ e^{-\lambda|\vec{r} - \vec{r}_p|} - a_- e^{-\lambda|\vec{r} - \vec{r}_m|}\Big) \\ & + f(\vec{r}) + \nabla^2 W + \mu W. \end{aligned} \tag{A.14}$$

The linear operator acting on $\vec{W} = (W \;\; \overline{W})^T$ is

$$\mathcal{L} = \begin{pmatrix} \mu - 2R_v^2 + \nabla^2 & -R_v^2 \\ -R_v^2 & \mu - 2R_v^2 + \nabla^2 \end{pmatrix}. \tag{A.15}$$

The inner product ensuring that $\mathcal{L}$ is self-adjoint operator is defined as

$$\langle F|G\rangle = \int_{-\infty}^{\infty}\int_{-\infty}^{\infty} \overline{F}(x', y')\, G(x', y')\, dx'\, dy'. \tag{A.16}$$

The linear Eq. (A.14) can be written compactly as $\mathcal{L}\vec{W} = \vec{\Phi}$, where

$$\Phi = -\dot{\vec{r}}_0 \cdot (\nabla R_v) - \mu a(\vec{r}) - R_v g(\vec{r}) - f(\vec{r}) + 3R_v^2 a(\vec{r}) - \lambda^2 a(\vec{r}), \tag{A.17}$$

and

$$a(\vec{r}) = a_+ e^{-\lambda|\vec{r}-\vec{r}_p|} - a_- e^{-\lambda|\vec{r}-\vec{r}_m|}. \tag{A.18}$$

According to the Fredholm alternative [4], solutions of $\mathcal{L}\vec{W} = \vec{\Phi}$ must satisfy the condition

$$\langle \Theta \mid \Phi \rangle = 0, \tag{A.19}$$

where Θ denotes any element of the kernel of the linear operator, that is, any function satisfying $\mathcal{L}\Theta = 0$. By analyzing the structure of $\mathcal{L}$ and exploiting the symmetries associated with spatial translations and phase invariance, one finds that the elements of the kernel of the adjoint operator $\mathcal{L}^\dagger$ are

$$\vec{\Theta}_1 = \begin{pmatrix} \partial_x R_v \\ \partial_x R_v \end{pmatrix}, \quad \vec{\Theta}_2 = \begin{pmatrix} \partial_y R_v \\ \partial_y R_v \end{pmatrix}, \quad \vec{\Theta}_3 = \begin{pmatrix} R_v \\ -R_v \end{pmatrix}. \tag{A.20}$$

Applying condition (A.19) yields two solvability conditions for the components of $\dot{\vec{r}}_0$:

$$\begin{aligned} &\Big\langle \partial_x R_v \,\Big|\, -\dot{\vec{r}}_0 \cdot (\nabla R_v) - \mu a(\vec{r}) - R_v g(\vec{r}) - f(\vec{r}) \\ &\qquad + 3R_v^2 a(\vec{r}) - \lambda^2 a(\vec{r}) \Big\rangle = 0, \\ &\Big\langle \partial_y R_v \,\Big|\, -\dot{\vec{r}}_0 \cdot (\nabla R_v) - \mu a(\vec{r}) - R_v g(\vec{r}) - f(\vec{r}) \\ &\qquad + 3R_v^2 a(\vec{r}) - \lambda^2 a(\vec{r}) \Big\rangle = 0. \end{aligned} \tag{A.21}$$

Changing to a reference frame in which the peripheral vortices are fixed, the term $-\dot{\vec{r}}_0 \cdot (\nabla R_v)$ becomes proportional to the central vortex's velocity components (v_x, v_y). For the configuration in which the three vortices are aligned along the $\hat{x}$-axis, straightforward calculations yield

$$v_x(x) = \gamma_1 g_2(x) + \big(\gamma_4 f_2(x) - \gamma_2 \tilde{a}_\pm(x)\big)\mu^{-1/2} + \gamma_3 \tilde{a}_\pm(x)\mu^{1/2}. \tag{A.22}$$

Introducing $\Delta = x - x_m$, where x and x_m denote the positions of the central and negative vortex, respectively, we obtain Eq. (11)

$$\dot{\Delta} = \Gamma_1(\Delta) + \Gamma_2(\Delta)\mu_0^{-1/2} + \Gamma_3(\Delta)\mu_0^{1/2}, \tag{A.23}$$

with

$$\Gamma_1(\Delta) = \gamma_1 g_2(\Delta + x_m), \tag{A.24}$$

$$\Gamma_2(\Delta) = \gamma_4 f_2(\Delta + x_m) - \gamma_2 \tilde{a}_\pm(\Delta + x_m), \tag{A.25}$$

$$\Gamma_3(\Delta) = \gamma_3 \tilde{a}_\pm(\Delta + x_m). \tag{A.26}$$

The specific values of γ_1, γ_2, γ_3 and γ_4, the specific definitions for f_2 and g_2, and all the intermediate calculations can be found on Supplemental Material 1.

References

[1] Cross MC, Hohenberg PC. Pattern formation outside of equilibrium. Rev Mod Phys 1993;65(3):851.
[2] Newell AC. Solitons in mathematics and physics. Society for Industrial and Applied Mathematics; 1985.
[3] Remoissenet M. Waves called solitons: concepts and experiments. Springer; 2013.
[4] Pismen LM. Patterns and interfaces in dissipative dynamics. Springer; 2006.
[5] Purwins HG, Bodeker HU, Amiranashvili S. Dissipative solitons. Adv Phys 2010;59(5):485–701.
[6] Descalzi O, Clerc MG, Residori S, Assanto G. Localized states in physics: solitons and patterns. Springer; 2011.
[7] Akhmediev N, Ankiewicz A. Dissipative solitons: from optics to biology and medicine. Springer; 2008.
[8] Tlidi M, Staliunas K, Panajotov K, Vladimiorv AG, Clerc MG. Localized structures in dissipative media: from optics to plant ecology. Philos Trans R Soc 2014;372(2027):20140101.
[9] Pismen LM. Vortices in nonlinear fields. Oxford University Press; 1999.
[10] Tsuneto T. Superconductivity and superfluidity. Cambridge University Press; 2005.
[11] Tinkham M. Introduction to superconductivity. Courier Corporation; 2004.
[12] Zilburg A, Rosenau P. On solitary patterns in lotka-volterra chains. J Phys A: Math Theor 2016;49(9):095101.
[13] de Gennes PG, Prost J. The physics of liquid crystals. Oxford University Press; 1993.
[14] Chandrasekhar S. Liquid crystals. Cambridge University Press; 1992.
[15] Fréedericksz V, Zolina V. Forces causing the orientation of an anisotropic liquid. Trans Faraday Soc 1927;29(140):919–30.
[16] Calisto E, Clerc MG, Zambra V. Magnetic field-induced vortex triplet and vortex lattice in a liquid crystal cell. Phys Rev Res 2020;2(4):042026.
[17] Clerc MG, Ferre M, Gajardo-Pizarro R, Zambra V. Dancing vortices in a driven nematic liquid crystal cell: theory and experiment. Phys Rev E 2022;106(1):L012201.

[18] Clerc MG, Gajardo-Pizarro R. Nullclines entanglement induced topological transitions in driven liquid crystal cells. Chaos Solit Fractals 2024;188:115447.
[19] Landau LD, Lifshitz EM. Statistical physics: volume 5. Elsevier; 2013.
[20] Belyaev VV. The viscosity of nematic liquid crystals. Russ Chem Rev 1989;58(10):917–47.
[21] Barboza R, Bortolozzo U, Clerc MG, Davila JD, Kowalczyk M, Residori S, et al. Light-matter interaction induces a shadow vortex. Phys Rev E 2016;93(5):050201.
[22] Barboza R, Bortolozzo U, Clerc MG, Residori S, Vidal-Henriquez E. Optical vortex induction via light-matter interaction in liquid-crystal media. Adv Opt Photon 2015;7(3):635–83.
[23] Barboza R, Bortolozzo U, Assanto G, Vidal-Henriquez E, Clerc MG, Residori S. Vortex induction via anisotropy stabilized light-matter interaction. Phys Rev Lett 2012;109(14):143901.
[24] Clerc MG, Vidal-Henriquez E, Davila JD, Kowalczyk M. Symmetry breaking of nematic umbilical defects through an amplitude equation. Phys Rev E 2014;90(1):012507.
[25] Clerc MG, Davila JD, Kowalczyk M, Smyrnelis P, Vidal-Henriquez E. Theory of light-matter interaction in nematic liquid crystals and the second painlevé equation. Calc Var 2017;56(4):93.
[26] Clerc MG, Kowalczyk M, Smyrnelis P. Symmetry breaking and restoration in the ginzburg-landau model of nematic liquid crystals. J Nonlinear Sci 2018;28(3):1079–107.
[27] Calisto E, Clerc MG, Kowalczyk M, Smyrnelis P. On the origin of the optical vortex lattices in a nematic liquid crystal light valve. Opt Lett 2019;44(12):2947–50.
[28] Gerrard A, Burch JM. Introduction to matrix methods in optics. Courier Corporation; 1994.
[29] Soskin MS, Denisenko VG, Egorov RI. Singular stokes-polarimetry as new technique for metrology and inspection of polarized speckle fields. In: Optical micro-and nanometrology in manufacturing technology; vol. 5458. SPIE; 2004, p. 79–85.
[30] Hariharan P. Optical interferometry. Academic Press; 2003.
[31] Barboza R, Sauma T, Bortolozzo U, Assanto G, Clerc MG, Residori S. Characterization of the vortex-pair interaction law and nonlinear mobility effects. New J Phys 2013;15(1):013028.